Research Article

ADVANCED PHOTONICS NEXUS

Chromatically resolved infrared light localization in a 3D chirped woodpile photonic structure

Eva Otero,[a,*] **Bertran Soria**,[a] **Mangirdas Malinauskas**,[b] **Darius Gailevičius**,[b] **Vygantas Mizeikis**,[c] **Saulius Juodkazis**,[d] **Kestutis Staliunas**,[a,e] **Jose Trull**,[a] **and Crina Cojocaru**[a]

[a]Universitat Politècnica de Catalunya, Department of Physics, Terrassa (Barcelona), Spain
[b]Vilnius University, Faculty of Physics, Laser Research Center, Vilnius, Lithuania
[c]Shizuoka University, Research Institute of Electronics, Hamamatsu, Japan
[d]Swinburne University of Technology, Optical Sciences Centre, Hawthorn, Australia
[e]Institució Catalana de Recerca i Estudis Avançats, Barcelona, Spain

Abstract. Engineering materials with tailored optical properties remain a key challenge in photonics. We report the design, fabrication, and experimental characterization of a three-dimensional chirped woodpile photonic crystal with nanometric features, produced via two-photon laser lithography. The structure exhibits wavelength-dependent light localization and intensity enhancement in the near-infrared regime, achieved through group velocity reduction. This effect arises from a gradual lattice-period chirp along the propagation direction, inducing a frequency-dependent bandgap shift and spatial separation of localized wavelengths. We propose an experimental technique capable of sensing the infrared light localization inside the crystal through the measurement of the transversely scattered light. We confirm, for the first time to our knowledge, strong localization in the 1400 to 1700 nm range, with longer wavelengths penetrating deeper into the crystal, consistent with numerical simulations. These findings open new opportunities for infrared photonic applications requiring enhanced light–matter interactions, including optical sensing, photoluminescence, advanced light sources, and nonlinear optical processes.

Keywords: light localization; 3D photonic crystal; chirped photonic structure; two-photon lithography.

Received Nov. 11, 2025; revised manuscript received Jan. 4, 2026; accepted for publication Jan. 26, 2026; published online Feb. 25, 2026.

[DOI: 10.1117/1.APN.5.2.026012]

1 Introduction

Progress in optical sensing and light detection technologies[1] is a major driver of very active research fields such as advanced microscopy techniques,[2] imaging,[3] spectroscopy,[4] and quantum information science.[5,6] For all these technologies, the development pathways are into wavelength ranges where light propagation management and detection techniques are not always fully available. Most of the proposals for future detectors are based on novel semiconductor heterostack devices,[7] sometimes comprising new materials with development that is usually complicated and features heavy metals and toxic processes.[8,9] Even successful manufacturing always deals with problems of miniaturization, wavelength discrimination, and bandwidth limitations. One interesting approach is not necessarily focused on the development of novel materials, but rather on the geometry engineering at the subwavelength scale using already established photonic materials, as different types of metamaterials, megastructures,[10] and photonic crystals (PhCs).[11] From bandgaps, stopgaps, tailored spectral or angular transmission and reflection, enhanced gain, or absorption, various effects can be controlled through the geometry design.[12] In general, this refers to spatial and temporal dispersion tailoring. In dielectric structures, particularly under conditions of low light intensity, these phenomena remain insufficiently investigated and may offer significant advantages for light confinement and detection applications.

Light localization within photonic structures is commonly achieved through the reduction of group velocity, which results in an increased electromagnetic energy density at specific

*Address all correspondence to Eva Otero, eva.otero@upc.edu

wavelengths and spatial regions inside the medium.[13] This enhancement of local field intensity significantly strengthens light–matter interactions, thereby enabling improved performance in applications such as nonlinear optics, sensing, and quantum photonics. Various strategies have been investigated to slow down the light using photonic architectures. Coupled resonator optical waveguides, for instance, significantly reduce group velocity, though they are constrained by the delay-bandwidth product, which needs a trade-off between slowing effects and operational bandwidth.[14–16] This limitation may be mitigated by chirping (gradually varying) the periodicity of a structure along the propagation direction, causing a frequency-dependent band gap shift. As a result, different wavelengths are stopped and reflected at different locations within the crystal, enabling chromatically resolved light localization, also known as the "trapped rainbow effect." This phenomenon has been demonstrated across different configurations, including dielectric[17] and plasmonic structures[18–21] gratings or waveguides designed in one-[22,23] and two-dimensional[24,25] PhCs, or in tapered[26] and in hyperbolic metamaterial waveguides.[27] Although they all show interesting results, several of these configurations, especially when metallic metamaterials are involved, show extrinsic losses, requiring gain media to maintain the efficiency.[28,29] To circumvent material losses, transparent dielectric alternatives operating in the metallic regime or active gain media can be employed,[30] yet challenges persist with out-of-plane radiation and scattering, particularly near the band edge, where slow-light effects are most pronounced.[30–34]

Experimental validations of the trapped rainbow effect have been conducted primarily in the microwave regime,[20,21,35,36] where both fabrication process and detection are simpler, and also in the visible frequencies using waveguides,[37,38] resonator arrays,[39] gratings,[19,40,41] and two-dimensional metasurfaces.[42,43] In this case, the modal volume of the localization is restricted by the geometry of the waveguide or grating, limiting local field intensity and the usable spectrally resolved volume. The concept has also been extended to acoustics[44,45] and very recently to topological rainbow effect designs.[46–49]

Despite previous studies on chromatically resolved trapping in one-dimensional (1D)[22] and two-dimensional (2D)[24,50] PhCs, three-dimensional (3D) configurations remain less explored. In Ref. 36, the authors numerically predicted rainbow trapping in a defect-free 3D PhC based on a woodpile architecture with an adiabatic lattice chirp, similar to the one proposed in this work. Although the theoretical analysis spans the optical domain, including visible and infrared wavelengths, experimental evidence is restricted to the microwave domain (5 to 10 GHz), where centimeter-scale periodicities facilitate fabrication and enable direct field measurements within the crystal. References 51 and 52 reported on the measurement of the stopbands in 3D photonic crystals, by measuring the reflectivity peaks across the front surface of the crystal. They reported observations of a shift in the stopband edges at different positions along the front surface of an inverse woodpile PhC, which employs etched pores instead of rods. This phenomenon observed here is unintentional and uncontrolled, and it is attributed to an unintended gradient in pore radii, arising from inherent variations introduced by the etching process.

Challenges in manufacturing optical-frequency 3D PhCs with sub-micrometer lattice periods are highlighted as a need for tuning photonic bandgaps (PBGs) to infrared (IR) and visible wavelengths. Most advanced micro- and nano-fabrication techniques used in planar semiconductor structuring struggle with the realization of functional 3D PhCs in the optical domain, even for spatially invariant structures without the lattice chirp, and it becomes nearly an impossible task for spatially variant chirped structures.

In this study, we undertake both theoretical and experimental investigations of chromatically resolved light trapping in the near-infrared (NIR) regime, and we demonstrate optical localization and intensity enhancement in the 1400 to 1700 nm range. We design and fabricate 3D woodpile chirped PhCs with sub-micrometer features using two-photon lithography (TPL), which has seen significant advancements during the last decades[53,54] and provides a reliable and promising solution for the very precise fabrication of complex 3D PhC structures at optical wavelengths.[55,56]

We predict and experimentally demonstrate wavelength-dependent light localization at different positions along the propagation direction. The novelty of our approach, compared with previous studies (Refs. 36, 51, and 52), lies in two key aspects: first, the successful fabrication of a 3D photonic crystal with sub-wavelength lattice periods; and second, the implementation of an original experimental technique capable of extracting wavelength-resolved light localization information from transversally scattered light. We believe that the spectral imaging results reported herein represent a significant advancement toward the challenging task of detecting light confinement within 3D photonic crystals.

2 3D Chirped Woodpile Photonic Crystal Design and Fabrication

We study a space-invariant 3D woodpile PhC consisting of a vertically stacked arrangement of layers, each formed by parallel dielectric rods, as schematically illustrated in Figs. 1(a) and 1(b). They are known to feature photonic stop-gaps and be compatible with 3D laser lithography approaches,[57] especially for fast prototyping. The individual structural elements forming the woodpile architecture usually exhibit an elliptical cross-sectional geometry, resembling the voxel-like[58] units employed in its fabrication. This geometric characteristic has implications for the choice of achievable design discussed later.

The TPL opto-mechanical setup used in this study, sketched in Fig. 1(c), employed a frequency-doubled Yb:KGW femtosecond laser (Carbide, Light Conversion, Vilnius, Lithuania) operating at a central wavelength of 515 nm, with pulse durations of 280 fs and a repetition rate of 60 kHz. The laser beam was focused into the bulk of a thick photoresist film using an oil immersion lens with a numerical aperture NA = 1.42. Optical exposure was achieved through localized two-photon absorption induced locally within the focal region of the focused laser beam. By exploiting both the optical nonlinearity of two-photon absorption and the threshold-like chemical nonlinearity of the photopolymerization process, the feature size can be reduced below the diffraction limit of the focusing lens. Under the experimental conditions, including laser wavelength, repetition rate, numerical aperture, and choice of photoresist, the average laser beam power required to produce photopolymerized structures with lateral dimensions of 100 to 200 nm ranged from 10 to 20 μW.

For extended 3D woodpile structures fabrication, the sample was precisely manipulated via an XYZ nanopositioning system (Aerotech ANT95L and ANT130LZS, Pittsburgh, Pennsylvania, United States), scanning along a predefined 3D trajectory at a speed of 200 μm/s. As 3D woodpile PhCs consist of

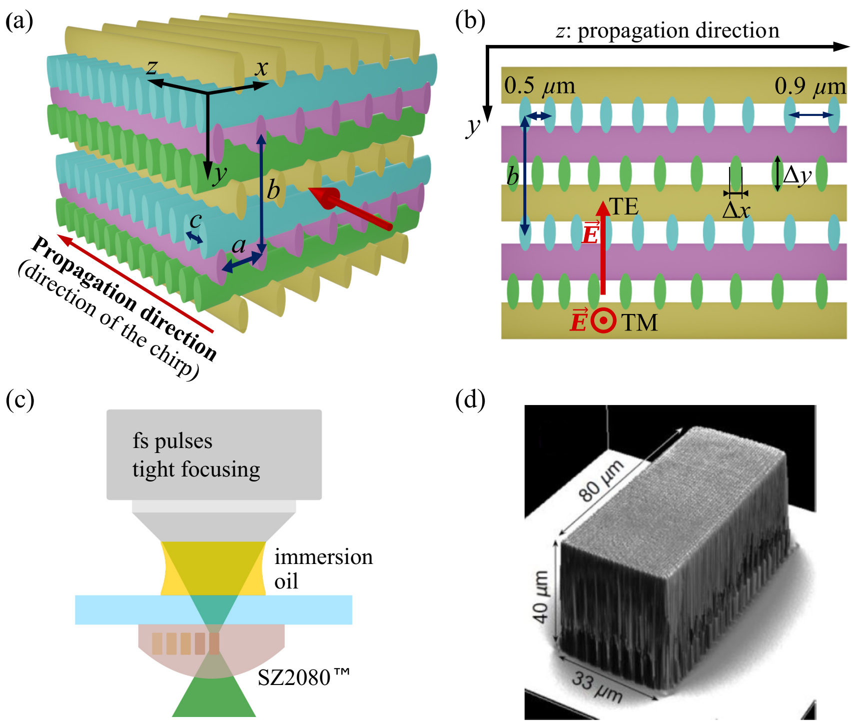

Fig. 1 (a) Schematic representation of the woodpile PhC scheme. All the rods are made of the same material, and the coloring is simply used to distinguish different layers. (b) Representation of the (y, z) transverse plane to the propagation direction, where the chirp and half-period shift between two consecutive layers are visible. (c) Fabrication setup sketch. (d) Representation and size of the whole crystal.

quasiperiodic (chirped) arrangements of dielectric rods, the fabrication process predominantly involved linear scans of the sample position. The initial material employed for TPL was the hybrid organic-inorganic photoresist SZ2080™, which is widely utilized in high-resolution 3D microfabrication due to its optical transparency and favorable mechanical properties. A photoinitiator, typically used to tune spectral sensitivity to the laser wavelength, was not required in this case as the intrinsic photosensitivity of SZ2080™ was sufficient to enable TPL without additional components. Omitting the photoinitiator allowed for further refinement of polymerized feature sizes while minimizing the proximity effect, which can lead to unintended structural connections between closely spaced elements. After the TPL fabrication, the samples were chemically developed in methyl isobutyl ketone (MIBK), followed by ethanol rinsing. To prevent structural collapse due to capillary forces acting on the delicate polymerized rods, the samples were dried using a critical point dryer (JCPD-5, JEOL) with liquefied CO_2, ensuring stability and structural integrity.

The geometric parameters of the fabricated crystal (structure dimensions, lattice periods, and chirp parameter) were determined from profilometer measurements on the top surface. A scanning electron characterization and discussion are provided in Sec. 1 in the Supplementary Material. These parameters, together with the refractive index ($n = 1.52$), were implemented in finite-difference time-domain (FDTD) numerical simulations to refine the design. Details of the FDTD methodology will be discussed in the following sections. A key design requirement was ensuring that the structure exhibited an experimentally observable rainbow trapping effect in the NIR wavelength range. Numerical analysis indicated that the effect can be achieved in the 1300 to 1800 nm range when the lattice periods along the x- and y-axis are $a = 0.94$ μm and $b = 1.92$ μm, respectively. Along the z-axis, which defines the chirp direction, the lattice period increases progressively from $c_0 = 0.5$ μm at the front plane to $c_f = 0.9$ μm at the back plane of the structure. For an accurate representation of the structural characteristics of the woodpile fabricated via the TPL method, the rods are assumed to have an elliptical cross-section with in-plane (minor) and vertical (major) diameters of $\Delta x = 0.3$ μm and $\Delta y = 0.78$ μm, respectively. The elliptical shape and axial elongation, by a factor of ∼2.5 to 2.8, arise due to the elongation of the focal region of the writing laser beam when focused by a high NA lens. The ellipticity of the rods was accounted for in our simulations. However, slight variations in this ellipticity due to fluctuations in laser power can alter the effective refractive index, further contributing to the minor spatial shifts observed in the localization peaks.

The total length of the structure is 84 μm, consisting of 120 periods, with an average increment of 3.3 nm per layer. The fabricated samples have an in-plane size of 30 μm $(x) \times 40$ μm (y), sufficiently large to allow the transmission of a collimated test beam without clipping. Thus, the final structure dimensions are 30 μm $(x) \times 40$ μm $(y) \times 84$ μm (z), as shown in Fig. 1(d).

2.1 Dispersion Analysis

The rainbow trapping mechanism relies on two key factors: the reduction of group velocity (v_g), which slows light propagation, and the presence of a photonic stop gap, which causes reflection. In PhCs, these conditions typically arise at frequencies near the PBG. When an adiabatic chirp is introduced into the crystal lattice, different wavelengths experience these effects at different depths within the structure.

The first and most critical step in designing the PhC samples was determining the conditions necessary for group velocity reduction in a perfectly periodic PhC (i.e., an infinite, spatially invariant, and nonchirped woodpile structure). In this initial study, the photonic band structure and group velocity were calculated using the plane-wave expansion method. Figure 2(a) presents the simulated photonic band structure based on the above-specified structural parameters. As the study primarily focuses on light propagation along the z-axis, the relevant modes are those with $k = (0, 0, k_z)$, corresponding to the $\Gamma - K_1$ segment in Fig. 2(a). Within this direction, the narrow frequency range marked in red exhibits no propagating modes, indicating the presence of a PBG.

The group velocity for light propagating along the z-axis was calculated through numerical differentiation of the dispersion relationships:

$$v_{\{g,z\}}(k_z) = \left(\frac{\partial\omega}{\partial k_z}\right)_{k_z} \approx \frac{\omega(k_z + dk_z) - \omega(k_z - dk_z)}{2dk_z}.$$

Given that the period in the chirped samples increases linearly with the position inside the crystal from $c = 0.5$ to 0.9 μm, we can determine the evolution of the PBG spectral edges along the z-axis and study how light propagates inside the PhC by looking at the evolution of the PBG with c. Figure 2(b) illustrates how the gap upper boundary in wavelength (corresponding to the lower boundary of the gap in frequency, Fig. 2(a) marked PBG) varies as a function of c parameter for the highest wavelength in TE and TM polarized modes. As shown in Fig. 1(b), TE modes are polarized parallel to the y-axis, whereas TM-like modes are oriented along the x-axis. Our study considers both TE and TM incident field polarization. However, in a 3D PhC, one cannot strictly talk about "TE" or "TM" modes due to mode mixing; for this reason, we will use the terms TE-like and TM-like.

As the gap behavior differs significantly between the two polarizations, TE- and TM-like modes are expected to propagate differently within the PhC. This is due to the lack of 90 deg rotational symmetry along the z-axis of the woodpile crystal. As shown in Fig. 2(b), light at $\lambda = 1500$ nm initially propagates freely within the crystal as it lies above the PBG boundary. However, as it penetrates deeper, the PBG shifts toward longer wavelengths until it reaches 1500 nm. At this point, the group velocity approaches zero, leading to localization of the light. For TM-polarized light, this occurs at $z = 17$ μm, whereas for TE-polarized light, localization occurs at $z = 23$ μm. For longer wavelengths, such as $\lambda = 1700$ nm, propagation continues deeper into the structure before reaching localization at $z = 42$ μm for TM-like modes and $z = 50$ μm for TE-like modes.

Figure 2(c) presents the evolution of group velocity as a function of lattice period and position inside the photonic crystal for

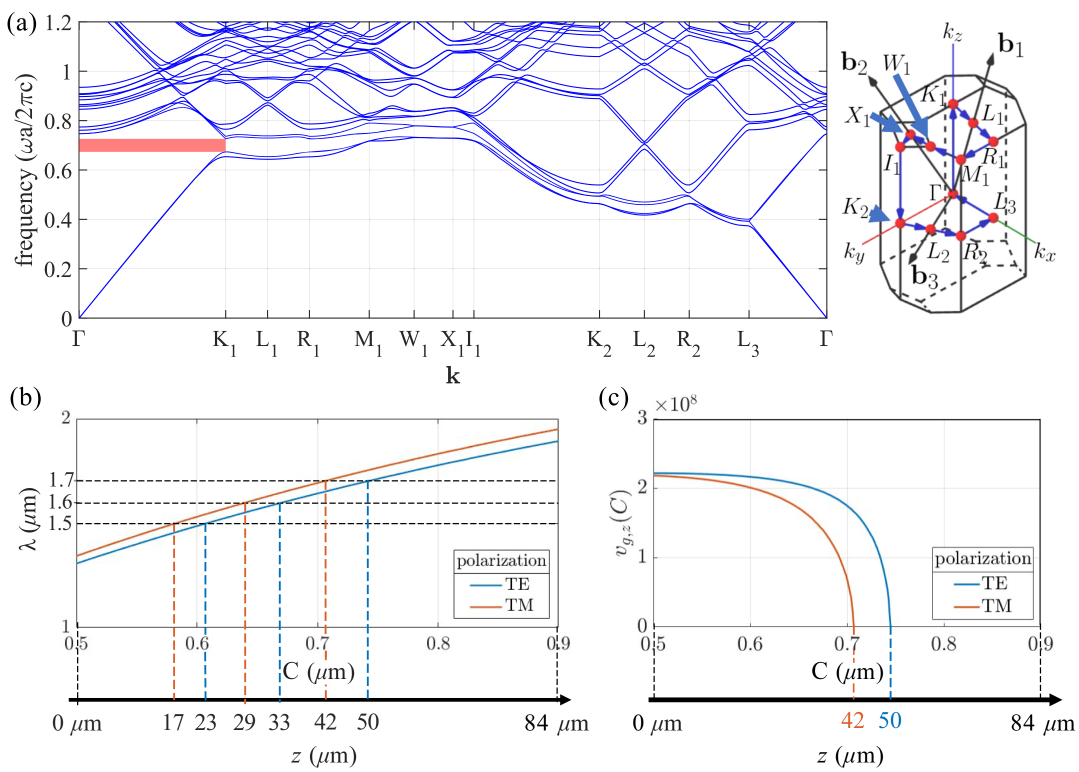

Fig. 2 (a) Computed PBS for a 3D woodpile for TE-like and TM-like modes. The red rectangle highlights the PBG seen by the light propagating along the z-axis. The right inset shows the first Brillouin zone of the lattice. (b) Evolution of the beginning of the PBG as the period c changes along the propagation direction z. (c) Evolution of the group velocity as a function of the period and the position inside the PhC for wavelength $\lambda = 1700$ nm.

$\lambda = 1700$ nm. Comparing this with Fig. 2(b) reveals that the group velocity decreases progressively as the wavelength approaches the bandgap edge, ultimately reaching zero at the PBG boundary.

The results in Fig. 2 indicate that the woodpile PhC with an increasing lattice period along the propagation direction exhibit optical localization at wavelengths above the photonic stop-gap boundary. Furthermore, the localization depth increases with wavelength.

2.2 Electric Field Intensity Distribution

To gain insight into the light propagation within the chirped PhC structures of finite length, numerical simulations were conducted using the FDTD method. We consider a finite crystal in the z-axis (simulating the whole length of our fabricated sample), and a single unit cell in the xy plane $(a \times b)$, normal to the propagation direction. We impose periodic boundary conditions in the xy plane while using perfectly matched layer (PML) boundary conditions at the z edges to minimize reflections and simulate an open boundary for outgoing waves. We consider the input electromagnetic field as a Gaussian source with a wavelength bandwidth from 1000 to 1700 nm. The beam has a plane wavefront and normal incidence on the xy plane.

Figure 3(a) presents the simulated distribution of normalized electric field intensity ($I \propto |E/E_0|^2$) inside the crystal as a function of propagation distance (z) for five distinct wavelengths in TE mode. This representation focuses on the xz plane for a fixed

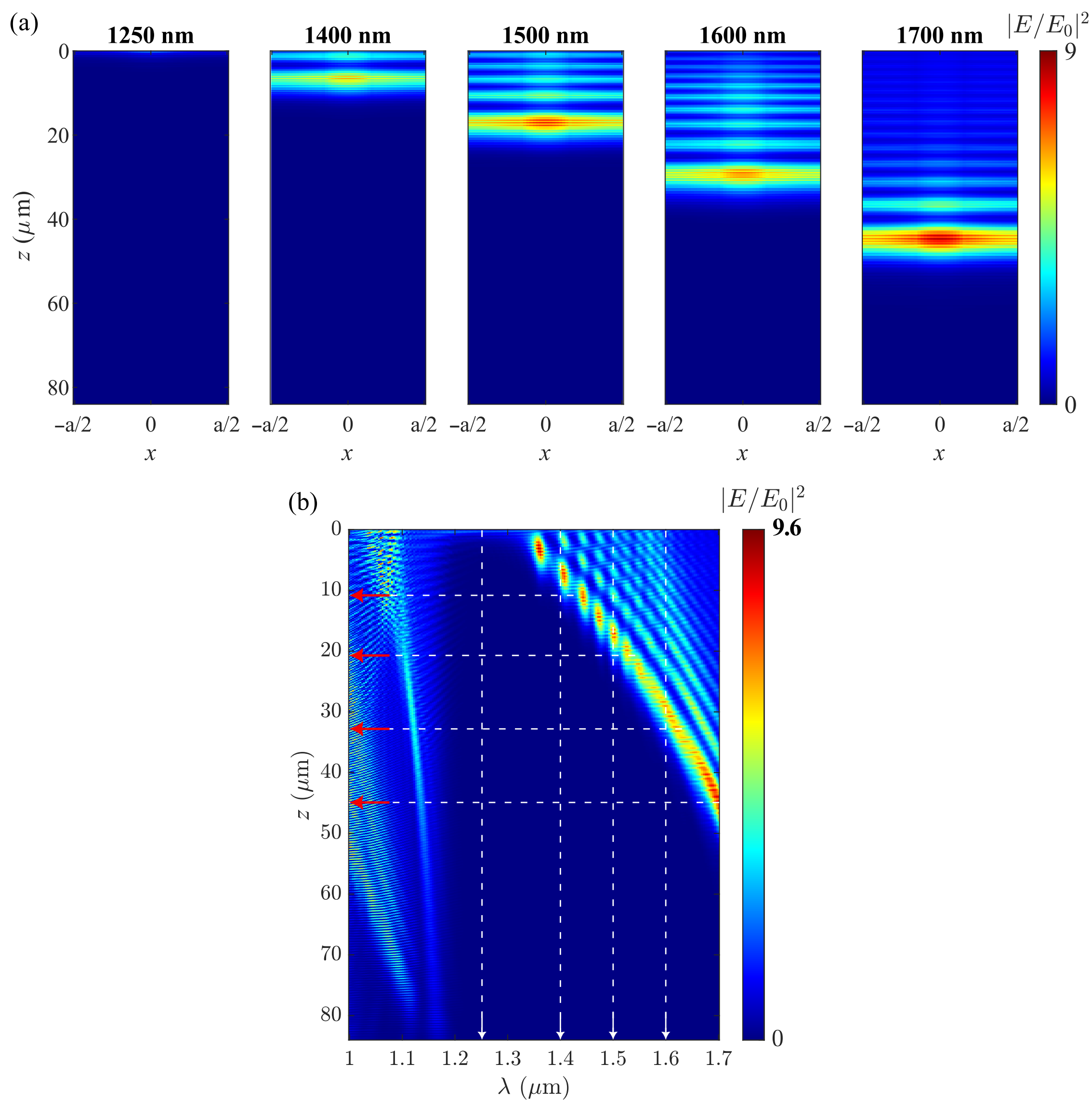

Fig. 3 (a) Electric field intensity distributions along propagation direction inside the crystal (from $z = 0$ to $z = 84$ μm) for one unit cell in the xy plane ($a \times b$), considering several wavelengths: $\lambda_1 = 1250$ nm, $\lambda_2 = 1400$ nm, $\lambda_3 = 1500$ nm, $\lambda_4 = 1600$ nm, and $\lambda_5 = 1700$ nm. (b) Electric field intensity spectral image along propagation direction for incident TE polarization. The wavelengths corresponding to Fig 3(a) are indicated in white arrows, and the localization z-position of each wavelength in red arrows.

y position. Although this analysis is conducted at a specific y coordinate, other y positions may exhibit different intensity distributions along the x-axis; however, the penetration depth along the z-axis remains consistent across these varying y positions. In addition, it should be emphasized that the horizontal axis (x) in this figure represents only one unit cell/period (a) of the structure. The colormap represents normalized electric field intensity values. As expected from Fig. 2(b), at $\lambda_1 = 1250$ nm, incident radiation is entirely reflected at the front face of the structure due to the presence of a PBG, preventing its penetration into the crystal. At longer wavelengths ($\lambda_2 = 1400$ nm, $\lambda_3 = 1500$ nm, $\lambda_4 = 1600$ nm, and $\lambda_5 = 1700$ nm), the radiation successfully enters the structure and is halted at progressively greater depths due to the gradual shift in the PBG.

This trend is further illustrated in Fig. 3(b), where the electric field intensity, at a central xy point, is mapped against wavelength and z-axis position. The resulting colormap represents the chromatically resolved rainbow-trapping effect along the whole crystal in the z-axis. Notably, the localization of light at wavelengths $\lambda_3 = 1500$ nm, $\lambda_4 = 1600$ nm, and $\lambda_5 = 1700$ nm ($z = 20$, 32, and 48 μm, respectively) occurs at z-coordinates closely matching the theoretical predictions ($z = 23, 33$, and 50 μm) derived from photonic band structure simulations in Fig. 2(b). The small variations are due to the fabrication tolerance of the structure.

3 Experimental Setup, Results, and Discussion

Measuring light propagation and intensity distribution within the PhC studied here presents a significant challenge due to the 3D geometry and sample size, which prevent direct probing of the internal electric field intensity. Although nano-detector concepts have been proposed,[59] integrating them into our 3D structure studied here is impractical. Instead, the characterization of the electric field intensity was conducted by measuring light scattered transversely to the propagation direction. We base our method on prior studies demonstrating that scattered light intensity at a given position correlates with the electric field intensity inside the crystal.[36]

To validate our experimental setup and establish the correlation between the measured transverse scattered light and the internal field distribution, we first conducted a reference experiment using two different diffusive glass samples, obtaining an exponential intensity decay consistent with the Beer–Lambert law (details in Sec. 2 of the Supplementary Material). This experiment validates the setup employed for measuring transverse scattered light, confirming that the recorded intensity is proportional to the internal intensity distribution within the crystal. Although this relationship is qualitatively reliable, the exact proportionality factor between the scattered light intensity and the corresponding internal field cannot be determined as no direct measurement method exists. Consequently, our approach enables only qualitative comparison with the internal intensity distribution. Nevertheless, to the best of our knowledge, this technique represents the most effective indirect probe for assessing wavelength-dependent light propagation and localization within the nanometric-scale 3D PhCs, and as shown below, our results exhibit strong qualitative agreement with numerical predictions.

3.1 Experimental Setup

A schematic representation of the experimental setup we built is shown in Fig. 4. The input light was provided by a supercontinuum fiber laser pumped at 1064 nm, emitting a broadband radiation within 450 to 1700 nm, with high spatial coherence and high spectral intensity. The supercontinuum seed, at $\lambda = 1064$ nm, was filtered out to prevent detector saturation. Input

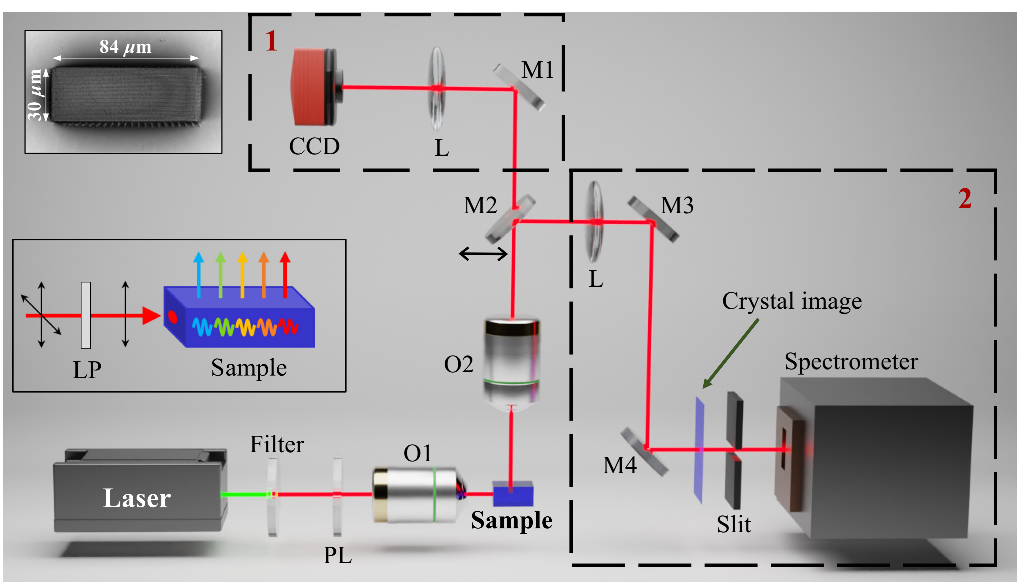

Fig. 4 Schematic representation of the experimental setup, where PL stands for linear polarizer; O1 and O2 are the first and second objectives; L is the lens; and M1, M2, and M3 are the mirrors (made using Ryo Mizuta Graphics). Paths 1 and 2 are marked by black dashed lines. The top left inset shows an image of the real sample and its dimensions. The middle left inset shows a close-up scheme of the polarized light coupled into the sample and the transversal scattered light.

polarization was controlled via a linear polarizer (PL). As the PhC is positioned at the very edge of the glass substrate, light was coupled into the structure using a long-working-distance, infinity-corrected 20×/0.42 microscope objective (O1). A CCD camera imaging the crystal's input face ensured optimal coupling quality. Light scattered upward from the chirped PhC was collected by a second microscope objective (O2) and could be directed along two distinct optical paths (path 1 and path 2).

3.2 Experimental Results and Discussion

3.2.1 Path 1: Spectrally filtered imaging

By moving the mirror M2 out of the optical path, scattered light was directed through a mirror (M1) and a lens (L1) onto an infrared CCD camera. Spectrally filtered images of the entire crystal were obtained by placing narrow bandpass filters [with 12 nm full width at half-maximum (FWHM)] in front of the CCD, isolating specific wavelength ranges from the supercontinuum laser spectra. The localization of different wavelengths, $\lambda_1 = 1350$ nm (FB1350-12 Thorlabs, Newton, New Jersey, United States), $\lambda_2 = 1400$ nm (FB1400-12 Thorlabs), and $\lambda_3 = 1600$ nm (FB1600-12 Thorlabs), within the crystal was recorded (Fig. 5).

As predicted by the simulations, wavelengths near the gap are localized at the front of the structure (1350 and 1400 nm), whereas longer wavelengths propagate deeper (1650 nm); thus, we observe good qualitative agreement between numerical simulations and experimental measurements. It should be noted that FDTD simulations in Fig. 3(a) show the intensity of the field on just one period in the x direction, whereas in the experimental results, we recorded the scattered light intensity of the whole crystal width, both in z and x directions, obtaining the scattered light distribution over many periods at once. The nine-factor enhancement predicted by the simulation cannot be experimentally retrieved as we are unable to make direct measurements of the field intensity inside the crystal. Nevertheless, the strong qualitative agreement of the light distribution gives us arguments to rely on the simulations and expect a similar enhancement factor.

3.2.2 Path 2: Spectral imaging via position filtering

This path directs the collected scattered light to a spectrometer (Andor Kymera 328i and iDus InGaAs camera), enabling spectral imaging at specific locations within the crystal. A system comprising three mirrors (M2, M3, and M4) and a $f = 1000$ mm tube lens (L) projects the image onto a 200 μm vertical slit, allowing only light from a selected z-axis position to enter the spectrometer for spectral analysis. To perform spatial scanning along z, mirror M4 was mounted on a stepper motor, enabling vertical displacement. By systematically adjusting its position, space-dependent spectra of scattered light were reconstructed along the propagation path inside the crystal, closely mirroring theoretical simulations. The black band centered at 1064 nm observed in the experimental plots corresponds to the filter used to block the supercontinuum seed.

Figure 6 shows the spectral image of light propagation along the crystal. Figure 6(a) shows the transverse scattered light measured by the spectral-imaging system for the TM-like mode; the colormap is presented on a logarithmic scale and normalized to the input laser spectral profile. Figure 6(b) shows the corresponding numerical predictions, as explained in the simulations in Fig. 3. As explained above, the simulations calculate the field intensity distribution within a single unit cell in the xy-plane and along the whole crystal in z-direction, whereas the experiments characterize the transverse scattered light from the entire crystal. Although the intensity scales in Figs. 6(a) and 6(b) are not directly comparable, the results qualitatively demonstrate wavelength-dependent light localization and intensity enhancement in the NIR range. The localization effect occurs for wavelengths above the PBG, with longer wavelengths penetrating deeper into the crystal, as indicated by the magenta arrow. Notably,

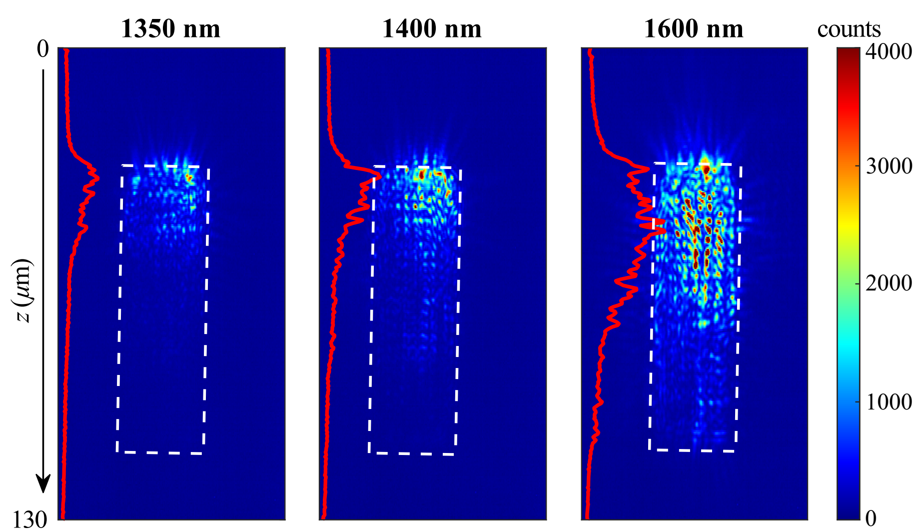

Fig. 5 (Spectrally filtered imaging.) Transverse scattered light images recorded with an infrared CCD camera, selecting three different narrow wavelength ranges around 1350, 1400, and 1600 nm using hard-coated bandpass filters. Red lateral curves show the integrated intensity along the propagation direction. Note that these results represent the transverse scattered light over the whole crystal width and length, and not the field intensity inside the crystal. The scale of the colormap corresponds directly to the CCD sensitivity.

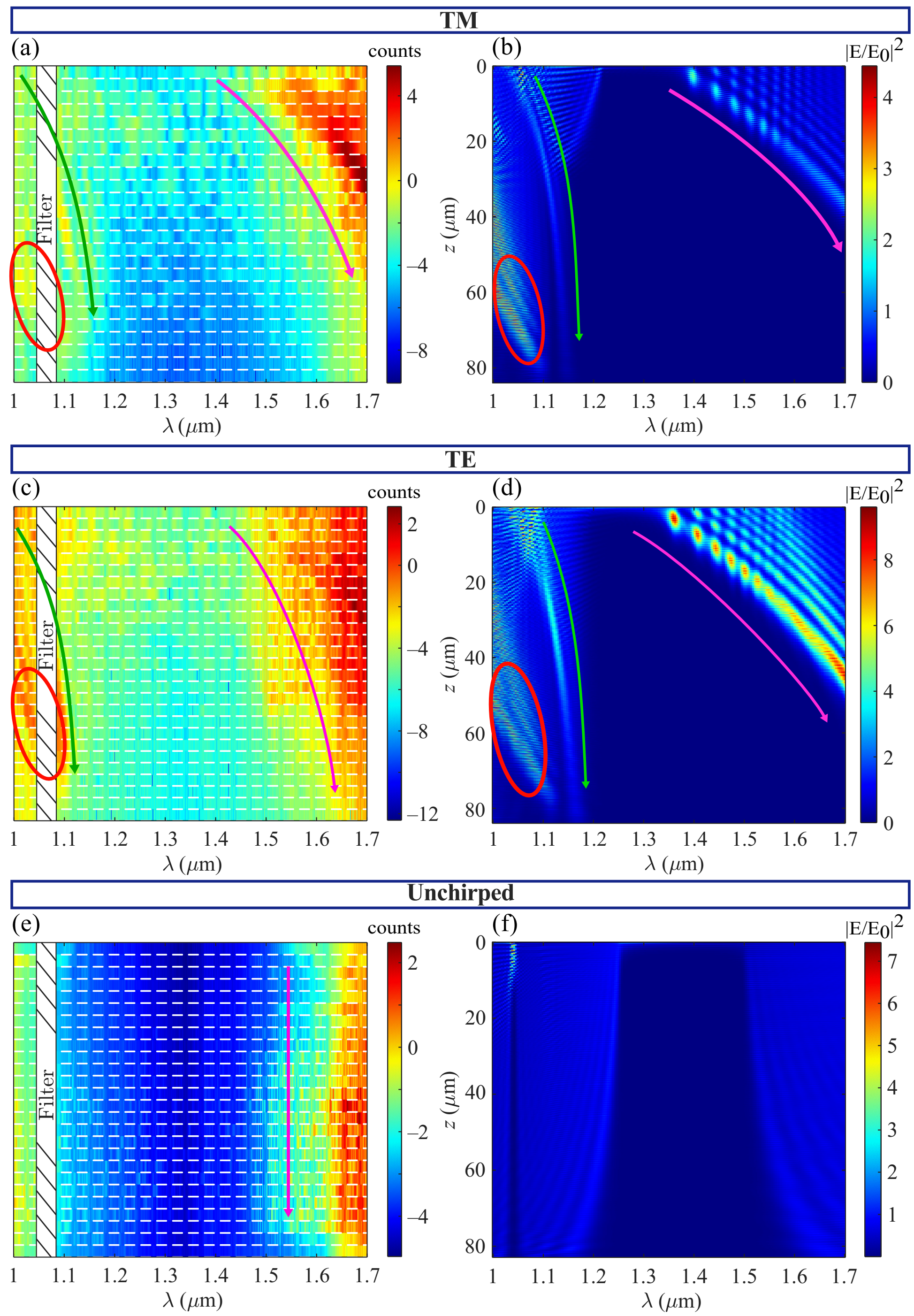

Fig. 6 (Spectral imaging via position filtering.) Experimental and numerical electric field intensity plots for TM-like (a), (b), TE-like (c), (d) chirped samples and unchirped sample (e), (f). Note that the color scale in the experimental results (a), (c), (e) is in logarithmic scale, and it represents the transverse scattered light as captured by the spectral imaging system. This measurement does not show the electric field intensity inside the crystal, unlike the simulations.

features below the gap seen in the simulations are also present in the experimental data, albeit at lower intensity (highlighted by the green lines and red circles). A similar behavior is observed for TE-polarized light, as shown in Figs. 6(c) and 6(d). Moreover, longer wavelengths exhibit greater penetration depth in TE-like mode compared with TM, aligning with the dispersion simulations [see Figs. 2(b) and 2(c)].

To confirm that the observed results originate from the chirped periodicity, we performed a comparative analysis using a nonchirped woodpile PhC with similar average structural parameters. As shown in Figs. 6(e) and 6(f), the unchirped sample does not exhibit wavelength-dependent light localization, and the PBG remains constant along the propagation direction.

4 Conclusion

We investigated light propagation in a chirped 3D woodpile photonic structure fabricated using TPL and successfully demonstrated chromatically resolved infrared light localization in the NIR spectral range. This work advances previous studies in two key directions:

First, we improve the fabrication process by producing high-quality 3D chirped woodpile geometries through TPL in a hybrid organic–inorganic photoresist, followed by a controlled shrinking step. This reduction in lattice periods to sub-micron dimensions is essential for observing the rainbow-trapping effect in the NIR regime.

Second, we introduce an original indirect sensing method for internal light localization based on transverse scattering light analysis. This approach addresses the challenge of directly measuring the internal optical field within sub-micrometric structures and enables the acquisition of high-quality spectral images of light distribution along the crystal's propagation direction.

The resulting scattered-light images show strong qualitative agreement with FDTD simulations, confirming the reliability of this technique for assessing wavelength-dependent spatial field distribution. Although the scattered-light intensity correlates qualitatively with the internal field intensity, the exact proportionality factor remains undetermined due to the absence of direct measurement methods. Despite this limitation, to the best of our knowledge, this technique represents the most effective indirect probe for studying wavelength-dependent light propagation and localization in nanometric-scale 3D photonic crystals.

As a next step, integrating fluorescent or nonlinear materials within the 3D photonic crystal could leverage the enhanced light–matter interactions enabled by chromatically resolved localization. Such integration would provide deeper insights into field localization and pave the way for promising applications, including optical sensing, photoluminescence enhancement, novel light sources, and nonlinear micro-photonic devices.

Disclosures

The authors declare that there are no financial interests, commercial affiliations, or other potential conflicts of interest that could have influenced the objectivity of this research or the writing of this paper.

Code and Data Availability

The data that support the findings of this article are available from the corresponding author upon reasonable request.

Acknowledgments

E.O., C.C., and J.T. acknowledge the Spanish Agencia Estatal de Investigacion from Ministerio de Ciencia, Investigacion y Universidades (project PID2023-148620NB-I00 granted by MICIU/AEI/'10.13039/501100011033 and FEDER, UE) and US Army Research Laboratory Cooperative Agreement No. W911NF-22-2-0236 issued by US ARMY ACC-APG-RTP. In addition, they acknowledge M. Scalora and R. Herrero for fruitful discussion. E.O. acknowledges the predoctoral program AGAUR-FISDUR (2023 FISDU 0050) of the Secretariat of Universities and Research of the Department of Research and Universities of the Generalitat of Catalonia and the European Social Plus Fund. M.M. acknowledges support of the research by the framework of the "Universities Excellence" Initiative program by the Ministry of Education, Science and Sports of the Republic of Lithuania under the agreement with the Research Council of Lithuania (Grant No. S-A-UEI-236). D.G acknowledges the ArtPM project from the Research Council of Lithuania (LMTLT), agreement No. S-MIP-24-10. K.S. acknowledges support by the Spanish Ministry of Science, Innovation, and Universities (MICINN) under the project PID2022-138321NB-C21.

References

1. A. Verma and B. C. Yadav, "Comprehensive review on two dimensional nanomaterials for optical biosensors: present progress and outlook," *Sustain. Mater. Technol.* **40**, e00900 (2024).
2. Y. U. Lee et al., "Metamaterial-assisted illumination nanoscopy with exceptional axial resolution," *Adv. Sci.* **11**, 2404883 (2024).
3. R. Guan et al., "Metamaterials for high-performance smart sensors," *Appl. Phys. Rev.* **11**, 041327 (2024).
4. Z. Zhao et al., "Applications of ultrafast nano-spectroscopy and nanoimaging with tip-based microscopy," *eLight* **5**, 1 (2025).
5. Y. Zhang et al., "Molecular and supramolecular materials: from light-harvesting to quantum information science and technology," *J. Phys. Chem. Lett.* **15**, 3294–3316 (2024).
6. J. Almutlaq et al., "Engineering colloidal semiconductor nanocrystals for quantum information processing," *Nat. Nanotechnol.* **19**, 1091–1100 (2024).
7. N. Qu et al., "Multi-scale design of metal–organic framework metamaterials for broad-band microwave absorption," *Adv. Funct. Mater.* **35**, 2402923 (2025).
8. J. Song et al., "Direct gas phase synthesis of high-purity black arsenic phosphorus with non-metallic mineralizer," *J. Alloys Compd.* **956**, 170256 (2023).
9. J. F. Da Silveira Petruci, D. Da Silva Sousa, and B. Mizaikoff, "Advanced mid-infrared sensors for molecular analysis," *Anal. Chem.* **97**, 6871–6890 (2025).
10. S. Sun et al., "Electromagnetic metasurfaces: physics and applications," *Adv. Opt. Photonics* **11**, 380 (2019).
11. C. T. Chan, K. M. Ho, and C. M. Soukoulis, "Photonic band gaps in experimentally realizable periodic dielectric structures," *Europhys. Lett.* **16**, 563–568 (1991).
12. J. W. Haus, "A brief review of theoretical results for photonic band structures," *J. Mod. Opt.* **41**, 195–207 (1994).
13. T. F. Krauss, "Why do we need slow light?," *Nat. Photonics* **2**, 448–450 (2008).
14. L. V. Hau et al., "Light speed reduction to 17 metres per second in an ultracold atomic gas," *Nature* **397**, 594–598 (1999).
15. A. V. Turukhin et al., "Observation of ultraslow and stored light pulses in a solid," *Phys. Rev. Lett.* **88**, 023602 (2001).
16. D. Smith et al., "Coupled-resonator-induced transparency," *Phys. Rev. A* **69**, 063804 (2003).
17. K. Totsuka, N. Kobayashi, and M. Tomita, "Slow light in coupled-resonator-induced transparency," *Phys. Rev. Lett.* **98**, 213904 (2007).
18. Q. Gan, Y. J. Ding, and F. J. Bartoli, ""Rainbow" trapping and releasing at telecommunication wavelengths," *Phys. Rev. Lett.* **102**, 056801 (2009).
19. Q. Gan and F. J. Bartoli, "Surface dispersion engineering of planar plasmonic chirped grating for complete visible rainbow trapping," *Appl. Phys. Lett.* **98**, 251103 (2011).
20. Y. Yang et al., "Trapping surface plasmon polaritons on ultrathin corrugated metallic strips in microwave frequencies," *Opt. Express* **23**, 7031–7037 (2015).
21. X. Gao et al., "Ultrathin dual-band surface plasmonic polariton waveguide and frequency splitter in microwave frequencies," *Appl. Phys. Lett.* **102**, 151912 (2013).

22. S. Elshahat and C. Lu, "Bidirectional rainbow trapping in 1-D chirped topological photonic crystal," *Front. Phys.* **10**, 831203 (2022).
23. A. H. Gevorgyan, N. A. Vanyushkin, and M. S. Rafayelyan, "Light localization in 1D chirped photonic crystals," *Eur. Phys. J. Plus* **137**, 719 (2022).
24. R. Engelen et al., "Two regimes of slow-light losses revealed by adiabatic reduction of group velocity," *Phys. Rev. Lett.* **101**, 103901 (2008).
25. H. Kurt and D. Yilmaz, "Rainbow trapping using chirped all-dielectric periodic structures," *Appl. Phys. B* **110**, 411–417 (2013).
26. K. L. Tsakmakidis, A. D. Boardman, and O. Hess, "'Trapped rainbow' storage of light in metamaterials," *Nature* **450**, 397–401 (2007).
27. H. Hu et al., "Rainbow trapping in hyperbolic metamaterial waveguide," *Sci. Rep.* **3**, 1249 (2013).
28. L. Chen et al., "Trapping of surface-plasmon polaritons in a graded Bragg structure: frequency-dependent spatially separated localization of the visible spectrum modes," *Phys. Rev. B* **80**, 161106 (2009).
29. A. Reza, M. M. Dignam, and S. Hughes, "Can light be stopped in realistic metamaterials?," *Nature* **455**, E10–E11 (2008).
30. J. He et al., "Slow light in a dielectric waveguide with negative-refractive index photonic crystal cladding," *Opt. Express* **16**, 11077–11082 (2008).
31. S. Hughes et al., "Extrinsic optical scattering loss in photonic crystal waveguides: role of fabrication disorder and photon group velocity," *Phys. Rev. Lett.* **94**, 033903 (2005).
32. S. Ek et al., "Slow-light-enhanced gain in active photonic crystal waveguides," *Nat. Commun.* **5**, 5039 (2014).
33. L. O'Faolain et al., "Dependence of extrinsic loss on group velocity in photonic crystal waveguides," *Opt. Express* **15**, 13129–13138 (2007).
34. L. O'Faolain et al., "Loss engineered slow light waveguides," *Opt. Express* **18**, 27627–27638 (2010).
35. Y. J. Zhou and T. J. Cui, "Broadband slow-wave systems of subwavelength thickness excited by a metal wire," *Appl. Phys. Lett.* **99**, 101906 (2011).
36. Z. Hayran, H. Kurt, and K. Staliunas, "Rainbow trapping in a chirped three-dimensional photonic crystal," *Sci. Rep.* **7**, 3046 (2017).
37. V. N. Smolyaninova et al., "Experimental observation of the trapped rainbow," *Appl. Phys. Lett.* **96**, 211121 (2010).
38. V. N. Smolyaninova et al., "Trapped rainbow techniques for spectroscopy on a chip and fluorescence enhancement," *Appl. Phys. B* **106**, 577–581 (2012).
39. K. Dixon et al., "Tunable rainbow light trapping in ultrathin resonator arrays," *Light Sci. Appl.* **9**, 194 (2020).
40. Q. Gan et al., "Experimental verification of the rainbow trapping effect in adiabatic plasmonic gratings," *Proc. Natl. Acad. Sci. U. S. A.* **108**, 5169–5173 (2011).
41. N. Kazemi-Zanjani et al., "Multiwavelength surface-enhanced Raman spectroscopy using rainbow trapping in width-graded plasmonic gratings," *Adv. Opt. Mater.* **6**, 1701136 (2018).
42. J. Li et al., "Full-color enhanced second harmonic generation using rainbow trapping in ultrathin hyperbolic metamaterials," *Nat. Commun.* **12**, 6425 (2021).
43. D. Tua et al., "Imaging-based intelligent spectrometer on a plasmonic rainbow chip," *Nat. Commun.* **14**, 1902 (2023).
44. V. Romero-García et al., "Enhancement of sound in chirped sonic crystals," *Appl. Phys. Lett.* **102**, 091906 (2013).
45. Z. Tian et al., "Dispersion tuning and route reconfiguration of acoustic waves in valley topological phononic crystals," *Nat. Commun.* **11**, 762 (2020).
46. S. Elshahat et al., "Perspective on the topological rainbow," *Appl. Phys. Lett.* **119**, 230505 (2021).
47. S. E. Soliman et al., "Topological rainbow trapping," *Nat. Rev. Phys.* **7**, 409–424 (2025).
48. C. Lu et al., "On-chip nanophotonic topological rainbow," *Nat. Commun.* **13**(1), 2586 (2022).
49. C. Lu et al., "Topological rainbow concentrator based on synthetic dimension," *Phys. Rev. Lett.* **126**, 113902 (2021).
50. T. Baba et al., "Light localizations in photonic crystal line defect waveguides," *IEEE J. Sel. Top. Quantum Electron.* **10**, 484–491 (2004).
51. M. Adhikary et al., "Experimental probe of a complete 3D photonic band gap," *Opt. Express* **28**, 2683–2698 (2020).
52. M. Adhikary et al., "Observation of Cartesian light propagation through a three-dimensional cavity superlattice in a silicon photonic band gap crystal," *Phys. Rev. Res.* **6**, 043235 (2024).
53. E. Skliutas et al., "Multiphoton 3D lithography," *Nat. Rev. Methods Primers* **5**, 15 (2025).
54. H. Wang et al., "Two-photon polymerization lithography for optics and photonics: fundamentals, materials, technologies, and applications," *Adv. Funct. Mater.* **33**, 2214211 (2023).
55. E. Otero et al., "Rainbow light trapping in a chirped 3D woodpile photonic crystal," in *24th Int. Conf. Transp. Opt. Networks (ICTON)*, Bari, Italy, pp. 1–3 (2024).
56. H. Liu et al. "High-order photonic cavity modes enabled 3D structural colors," *ACS Nano* **16**, 8244–8252 (2022).
57. K. B. Samusev et al., "Optical properties of woodpile photonic crystals produced by three-dimensional laser lithography," *Phys. Solid State* **57**, 2494–2501 (2015).
58. L. Jonušauskas et al., "Mesoscale laser 3D printing," *Opt. Express* **27**, 15205 (2019).
59. T. Moein et al., "Optically-thin broadband graphene-membrane photodetector," *Nanomaterials* **10**, 407 (2020).

Eva Otero is a PhD researcher at the Universitat Politècnica de Catalunya (UPC). She holds a bachelor degree in physics from the Universitat Autònoma de Barcelona and a master degree in photonics from UPC. She is part of the Nonlinear Optics and Lasers laboratory within the DONLL research group. Her research centers on the experimental study of nanophotonics, focusing on light localization and enhancement in nanostructures and their linear and nonlinear applications.

Bertran Soria is a PhD researcher at the Institute of Photonic Sciences (ICFO). He holds a BSc degree in engineering physics and an MSc degree in photonics from the Universitat Politècnica de Catalunya (UPC). He currently is part of the Atomic Quantum Optics group, where he focuses on quantum sensing with cold atoms, with particular focus on magnetometry for exotic forces. His prior work concentrated on experimental nanophotonics and nonlinear properties at UPC's DONLL research group.

Mangirdas Malinauskas is a chief researcher at Vilnius University's Laser Research Center, advancing laser 3D micro and nanostructuring of crosslinkable materials for applications in microoptics, nanophotonics, and biomedicine. His current work centers on nonlinear 3D nanolithography and multiphoton polymerization, contributing to the fabrication of functional inorganic materials. He maintains active international collaboration, including ongoing synergy with IESLFORTH, building on long-standing scientific ties with its photonics research groups.

Darius Gailevičius is a senior researcher at Vilnius University's Laser Research Center, advancing photonics and laser microfabrication technologies. His current work centers on femtosecond laser structuring and computational optics, contributing to the manufacturing of functional inorganic materials and resilient micro-optical components. He maintains active international collaboration, working with global partners to develop novel light manipulation techniques and spatially structured laser systems.

Vygantas Mizeikis is a professor at Shizuoka University's Research Institute of Electronics, working at the interface of photonics and advanced manufacturing. His research focuses on ultrafast laser–matter interaction and femtosecond-laser micro/nanofabrication—direct-write lithography and laser ablation—to realize 2D/3D photonic crystals, metasurfaces, and structurally colored microoptical elements, supported by optical characterization and sensing. He earned a PhD in physics from Vilnius University in 1997 and has pursued his career in Japan, maintaining active international collaborations in Europe.

Saulius Juodkazis is a professor of nanophotonics and director of the Nanotechnology Facility (Nanolab) at Swinburne's Optical Sciences Centre. His current research is focused on applying principles of light-field enhancement and its spectral control for applications in micro-optics, sensing, solid-state lighting, and solar energy conversion. He has held previous tenured positions at the Universities of Tokushima and Hokkaido in Japan, and is the author of 700+ peer-reviewed journal papers, reviews, and several book chapters.

Kestutis Staliunas is an ICREA (Institució Catalana de Recerca i Estudis Avançats) professor in Department of Physics of Universitat Politecnica de Catalunya, Barcelona, head of the research group on micro-lasers, photonics, non-Hermitian systems, and nonlinear optical patterns. He is an author of more than 200 research articles with more than 9000 citations (h-factor 54), and has been invited to give more than 100 presentations at conferences. Up to now, he successfully directed (and currently directing) 20 PhD projects.

Jose Trull is a full professor at Universitat Politècnica de Catalunya and works in the research group of Nonlinear Dynamics, Nonlinear Optics, and Lasers. Currently, he coordinates the Nonlinear Optics and Lasers laboratory. His research activity is currently focused on experimental studies in nonlinear optics and photonics at the nanoscale. He is co-author of several publications, co-inventor of a patent, and has participated in several financed competitive research projects and in the co-direction of several PhD thesis.

Crina Cojocaru is a full professor, in the Physics Department, Universitat Politècnica de Catalunya (UPC), and a member of the "Nonlinear Dynamics, Nonlinear Optics, and lasers" research group. She holds BSc and MSc degrees in physics from the University of Iasi, Romania, and a PhD in physics from UPC, Barcelona (2002). Her research covers different aspects of photonics, focused on nonlinear optics, with emphasis on nanophotonics. She co-authors over 100 scientific papers and is a co-inventor of one European patent.